# Jet delivery system for Raman scattering on bio-inorganic compounds

A. Wetzel, F. Biebl, K. R. Beyerlein, J. Stanek, L. Gumprecht, A. Hoffmann, S. Herres-Pawlis, S. Bajt, H. N. Chapman, B. Grimm-Lebsanft, D. Rukser, and M. Rübhausen

# Jet delivery system for Raman scattering on bio-inorganic compounds

A. Wetzel,[1,a)] F. Biebl,[1] K. R. Beyerlein,[2] J. Stanek,[3] L. Gumprecht,[2] A. Hoffmann,[3] S. Herres-Pawlis,[3] S. Bajt,[4] H. N. Chapman,[2,5,6] B. Grimm-Lebsanft,[1] D. Rukser,[1] and M. Rübhausen[1]

[1]*Institut für Nanostruktur- und Festkörperphysik, Universität Hamburg, Notkestrasse 85, 22607 Hamburg, Germany*
[2]*Center for Free-Electron Laser Science, Deutsches Elektronen-Synchrotron, Notkestrasse 85, 22607 Hamburg, Germany*
[3]*Institut für Anorganische Chemie, RWTH Aachen University, Landoltweg 1, 52074 Aachen, Germany*
[4]*Photon Science, DESY, Notkestrasse 85, 22607 Hamburg, Germany*
[5]*Centre for Ultrafast Imaging, Luruper Chaussee 149, 22761 Hamburg, Germany*
[6]*Department of Physics, Universität Hamburg, Luruper Chaussee 149, 22761 Hamburg, Germany*

We present a micro-jet sample delivery system for Raman measurements. Compared to cuvette measurements, the observed Raman signal is enhanced by more than one order of magnitude and does not contain signal distortions from the liquid-glass interface. Furthermore, the signal stability of repeated measurements is enhanced due to reduced sample damage effects by constantly replenishing the sample. This allows the study of sensitive samples that can only be produced in low concentrations. Our setup consists of a controlled sample environment that can be either under vacuum or an exchange gas, which allows the study of samples that are unstable in air. Finally, by matching the effective source point of the Raman instrument with the diameter of the jet, controlled experiments using laser beams of different wavelengths are possible. We see future applications of our setup for resonance Raman and time-resolved Raman measurements of bioinorganic samples. *Published by AIP Publishing.* [http://dx.doi.org/10.1063/1.4967476]

Copper is an important redox-active metal in many biological processes.[1–13] The structural imitation of active centers in bioinorganic chemistry allows the development of a synthetic catalyst inspired by an enzymatic mechanism.[1–10] The structure of many bioinorganic metal complexes is strongly connected with the charge-transfer mechanisms between different metal oxidation states.[1] The ligand-to-metal coordination can be studied by Raman spectroscopy.[1,14] Time-resolved measurements allow to study the detailed mechanisms of the charge-transfer processes.[1] UV Resonance Raman provides detailed information on donor-metal vibrations and insights into electronic and structural degrees of freedom. Since these samples are usually in solution, conventional methods of Raman measurements utilize a cuvette[1] or a flow cell selection. This results in small signals and a strong sensitivity to sample damage effects with relatively low laser powers. Also, the glass surface of a cuvette or flow cell is in direct contact with the liquid surface, resulting in distortions of the signal. In our new sample delivery system, we eliminate the interface between glass and cuvette under vacuum conditions, which leads to a significant signal improvement in a controlled sample environment. This makes it possible to achieve good signals at low sample concentrations resulting in low sample consumption during the Raman measurements. The sample damage effects are avoided by continuously replenishing the sample. These advantages allow us to perform longer measurements with many accumulations, which are necessary for the study of resonance and transient Raman measurements.

The experimental configuration used in our experiments is shown in Fig. 1, depicting the positioning of the chamber into the focal point of the reflective objective that couples the light into the UT-3 Raman spectrometer, which is a triple-grating deep ultraviolet to near-infrared instrument with two subtractively coupled monochromators acting as an optical bandpass filter in a wavelength range between 165 and 1000 nm.[15] The instrument is also capable of performing time resolved studies.[16] The reflection of the direct laser light
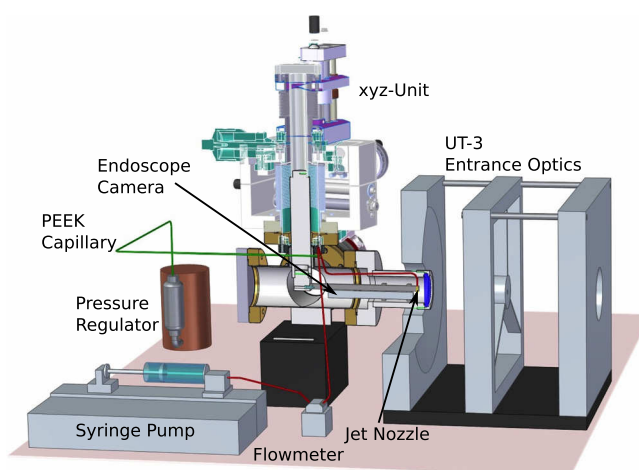


FIG. 1. CAD drawing of the jet chamber constructed for Raman measurements using the UT-3 Raman spectrometer. We display the entrance optics of UT-3 Raman spectrometer. This setup allows a sample delivery via a micro jet into the entrance optics of spectrometer. A sample delivery system to the nozzle for the sample injection inside the entrance optics and a jetting gas dynamic virtual nozzle with a jet diameter of 10 $\mu$m, recorded with the endoscope camera inside the jet chamber.

a)Electronic mail: atittel@physnet.uni-hamburg.de

from the jet was blocked by a beam block inside the entrance optics. More details on this experiment can be found in Schulz *et al.*[15] The vacuum chamber consisted of a stainless steel main body with an adapter for the entrance optics in front of it. A fused silica window at a distance of 5 mm from the jet was mounted in front of the adapter. It enabled an unhampered beam penetration into the chamber, but still allowing tight focusing onto the jet. A turbomolecular vacuum pump (Hi Pace 80, Pfeiffer) on the right side of the chamber can be connected to generate a vacuum. Alternatively, a controlled He/N$_2$ atmosphere in the chamber could be established. While there was no sample catcher inside the chamber, the vacuum pump also assured the evacuation of used sample. The measurement of the vacuum inside the chamber was carried out by a Pirani cold cathode (PKR 251, Pfeiffer). Best achievable pressure inside the chamber during the jet operation was $10^{-7}$ mbar. Fig. 1 shows the sample delivery system to the nozzle. Liquid was supplied to the nozzle using a middle-pressure syringe pump (Nemesys, cetoni) via a polyether ether ketone (PEEK) capillary. A pressure regulator controlled the pressure of the He gas supplied to the nozzle via a second PEEK capillary. The nozzle was located behind the window and was connected via a stainless bolt to an xyz-stage (Multi Base XY14). This stage was controlled by a micrometer screw, enabling a precise manual movement to facilitate an overlap of the jet with the UT-3 focal point (see Fig. 1). An endoscope camera (Supereyes® B003+) mounted behind the jet nozzle allowed the observation of the jet stability during the measurement. Hence, the endoscope camera facilitated the adjustment of the jet focus point. We used ceramic-based gas dynamic virtual nozzles[17] for generation of the micro jet.[18–28] To fit the nozzle to the jet chamber, we designed a special short nozzle with a 10-mm long ceramic piece. For the Raman measurements, we used a Millennia-Tsunami system (Spectra Physics) with a repetition rate of 80 MHz and a pulse energy of 15 nJ including flexible harmonic generation as a source for the photons incident on the sample and a UT-3 Raman spectrometer as analyzer of the scattered light. For steady state measurements, a wavelength of 425 nm [full width at half maximum (FWHM) is 1.8 ps, pulse energy = 0.9 nJ] for the Raman probe was used. To study the charge-transfer mechanisms of the samples, we employed a pump-probe configuration with a pump wavelength of 283 nm (FWHM = 1.7 ps, pulse energy = 0.29 nJ) and a probe wavelength of 425 nm (FWHM = 1.8 ps, pulse energy = 0.31 nJ). To validate the Raman setup, we used the biomimetic model complexes for the entatic state, which have been prepared using procedures from the literature.[1,29] These complexes consist of a Cu$^I$ center with the hybrid guanidine-quinoline ligands TMGqu or DMEGqu.[1,29] The center ion is bound to four nitrogen atoms, which belong to two quinoline and two guanidine groups. The dominant copper-core related vibration modes at 530 cm$^{-1}$ (Cu-N$_{qu}$) and 645 cm$^{-1}$ (Cu-N$_{gua}$ + Cu-N$_{qu}$) are highly relevant as they yield information on the structural distortions of the Cu-center.[1,6,29–32]

For the optimization of the Raman signal it was important to fit the jet size to the optical Raman spot size with regard to the measurements with the UT-3. We needed to optimize the laser power deposited into the jetting sample

without disrupting the jet. The spot size of the UT-3 Raman setup was adjusted to 20 $\mu$m. In order to increase the original micro-jet diameter of 2–5 $\mu$m,[17] we systematically changed certain jetting parameters. The micro jet diameter $D_j$ is given by[17–26]

$$D_j = \left[\frac{8\rho_l}{\pi^2\left(\alpha\rho_g - P_0\right)}\right]^{\frac{1}{4}} Q_l^{\frac{1}{4}} \qquad (1)$$

with $\rho_l$ the liquid viscosity, $\alpha$ the special velocity, $Q_l$ the liquid flow rate, $P_0$ pressure outside the nozzle and $\rho_g = \frac{Q_g}{A}$ momentum of the gas flow through the aperture per unit volume. The first step for jet diameter optimization was an optimization of gas flow and chamber pressure parameters. For the constant $\rho_l$ and $P_0$, we needed a minimization of the term $\alpha\rho_g$, where

$$\alpha = \sqrt{\frac{RT}{km_g}} \frac{\left(1 + \frac{k-2}{2}M^2\right)^{\frac{k+1}{2(k-1)}}}{M} \qquad (2)$$

with M as the Mach number of the gas flow through the aperture

$$M = \left(\left(\left(\frac{P_i}{P_0}\right)^{\frac{k-1}{k}} - 1\right)\frac{2}{k-1}\right)^{\frac{1}{2}} \qquad (3)$$

and $k = \frac{C_p}{C_v}$ the ratio of specific heat of the gas. $P_i$ is the pressure inside the nozzle, R denotes the ideal gas constant, T the temperature, and $m_g$ the molar mass of the gas. To maximize the jet diameter, $D_j$, we decreased $\alpha\rho_g$ by decreasing the gas flow, $Q_g$, and the parameter $\alpha$ (Eqs. (1) and (2). Minimizing $\alpha$ was done by minimizing the Mach number and increasing the chamber pressure, $P_0$ (Eq. (3)). For this reason, we have decreased the gas pressure to a minimum value of 200 Psi that still allowed the formation of the jet. To make the ambient pressure jet possible, we have built a sample unloading system consisting of a sample catcher under the nozzle, a sample transporting pipe and a reservoir for the used sample. For the further optimization of jet diameter, we have increased the liquid flow rate systematically. With a sample volume of 60 ml and a typical flow rate of 70 $\mu$l/min, a continuous measurement time of 15 h was possible. The optical spot diameter of 20 $\mu$m and the jet diameter of 10 $\mu$m resulted in a homogeneous illumination of the jet in our setup. The resulting Raman signal as a function of the flow rate is shown in Fig. 2(a).

Only sample flow rates in the range of 15 to 100 $\mu$l/min were achievable by the syringe pump used for the sample delivery. Elastic scattering can be seen in the measurement at low flow rates of 15 $\mu$l/min. This suggests that the jet starts to generate single drops at very low flow rates leading to scattering of the laser light in all directions, which cannot be blocked with a beam block inside the entrance optics. As shown in the Fig. 2, we observe a continuous rise of Raman signal with increasing flow rates. The sample peaks become sharper and rise from the background continuously. The typical structure of the Raman spectra for Cu(DMEGqu)$_2$PF$_6$ is clearly visible at 70 $\mu$l/min and at 100 $\mu$l/min in the figure.
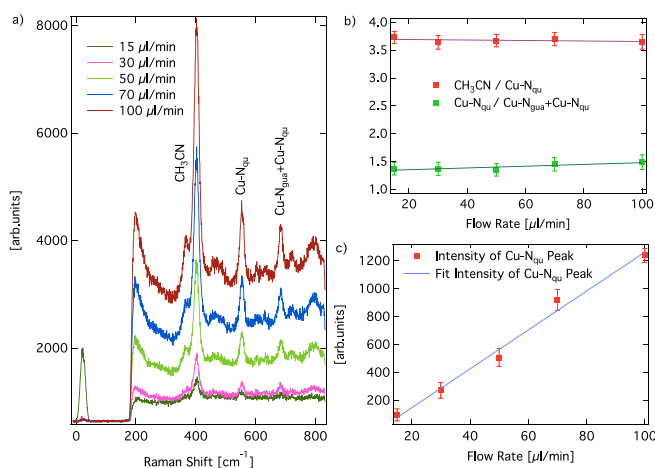
FIG. 2. (a) Flow rate dependence of Raman spectra of $Cu(DMEGqu)_2PF_6$. (b) The ratio between the solvent peak ($CH_3CN$) and the first sample peak ($Cu-N_{qu}$ mode) (red dots) with a linear fit (red line) and the ratio between the first ($Cu-N_{qu}$) and the second ($Cu-N_{gua} + Cu-N_{qu}$) sample peaks (green dots) with a linear fit (green line). (c) Absolute intensity of $Cu-N_{qu}$ mode in dependence on the flow rate (red dots) with a linear fit (blue line). The signal increases with the increasing liquid flow rate wherein the relation between the sample peaks remains constant. Measurements are performed with a laser energy of 2.92 eV (425 nm).

We have decided to use a 70 $\mu$l/min flow rate in the following measurements as a reasonable compromise between a signal quality and a possible jetting time, defined by the syringe volume and optimal working conditions of the syringe pump. We have analyzed three relevant vibration modes of the sample: solvent ($CH_3CN$) mode at 375 $cm^{-1}$ and two core vibration modes: $Cu-N_{qu}$ at 530 $cm^{-1}$ and $Cu-N_{gua} + Cu-N_{qu}$ at 645 $cm^{-1}$. The ratio between the solvent peak ($CH_3CN$) and the first $Cu-N_{qu}$ mode is constant as shown in Fig. 2(b). The ratio between the first $Cu-N_{qu}$ mode and the second $Cu-N_{gua} + Cu-N_{qu}$ mode is also constant in the Fig. 2(b). This provides information about the sample stability during the change of the flow rate. The peak intensity of the first $Cu-N_{qu}$ mode rises with the rising flow rate directly proportional as shown in Fig. 2(c). To optimize the intensity of the sample peaks in comparison to the solvent peaks, we have changed the concentration of the sample in the jet. As shown in Fig. 3, a low sample signal at 0.1 mM concentration develops as a strong signal at 3 mM. Concentrations above 3 mM were not possible to measure, as they would quickly clog the nozzle. The ratio between the solvent peak ($CH_3CN$) and the first $Cu-N_{qu}$ mode is constant as shown in Fig. 3(b). The ratio between the first $Cu-N_{qu}$ mode and the second $Cu-N_{gua} + Cu-N_{qu}$ mode is also constant in Fig. 3(b) indicating that the sample characteristic peaks are not modified by the changing concentrations. The peak intensity of the first $Cu-N_{qu}$ mode rises linearly with the increasing sample concentration as shown in Fig. 3(c).

The non-linear increasing proportion of the solvent peak to sample peak for lower sample concentrations might be explained by coordination of solvent with the sample. The penetration depth of a 425 nm wavelength laser for the maximum sample concentration is approximately 100 $\mu$m, which is at least one order of magnitude larger than the jet diameter. For all further measurements, we decided to use a 2 mM concentration of the $Cu^I$ sample to allow an optimized
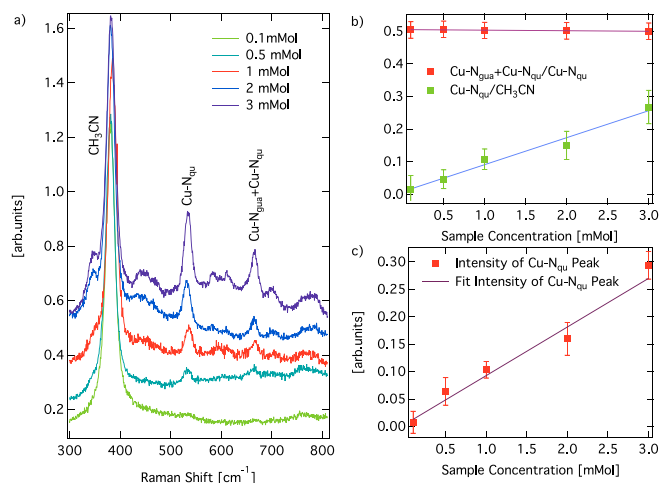


FIG. 3. (a) Steady-state Raman measurements of $Cu(DMEGqu)_2PF_6$ in jet with sample concentrations of 0.1 mM, 0.5 mM, 1 mM, 2 mM, and 3 mM. (b) The ratio between solvent peak ($CH_3CN$) and first sample peak ($Cu-N_{qu}$) (red dots) with a linear fit (red line) and the ratio between the first ($Cu-N_{qu}$) and the second ($Cu-N_{gua} + Cu-N_{qu}$) sample peak (green dots) with a linear fit (blue line). (c) Absolute intensity of $Cu-N_{qu}$ mode in dependence of the sample concentration (red dots) with a linear fit (black line). The signal increases with the increasing liquid flow rate wherein the relation between the sample peaks remains constant. Measurements have been performed with a laser energy of 2.92 eV (425 nm).

sample delivery through the nozzle and also to minimize the clogging processes. To determine the damage thresholds, we have recorded the dependence of steady state Raman spectra on laser power in the power range from 5 mW to 70 mW. As shown in the Figs. 4(a) and 4(b), the laser signal increases linearly without signal saturation directly proportional to the laser power. The ratios between sample characteristic peaks and solvent peaks are also not affected by the changed laser power as shown in the Fig. 4(b).
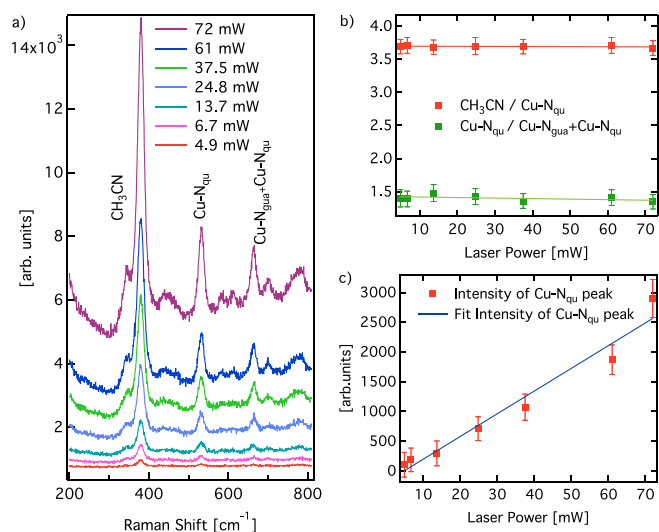


FIG. 4. (a) Dependence of the steady-state Raman spectra of $Cu(DMEGqu)_2$ $PF_6$ of the laser power. (b) The ratio between solvent peak ($CH_3CN$) and the first sample peak ($Cu-N_{qu}$) (red dots) with a linear fit (red line) and the ratio between first ($Cu-N_{qu}$) and the second sample peak ($Cu-N_{gua} + Cu-N_{qu}$) (green dots) with a linear fit (green line). (c) Absolute intensity of $Cu-N_{qu}$ mode in dependence of the laser power (red dots) with a linear fit (blue line). The signal increases with the increasing laser power wherein the relation between the sample peaks remains constant.

For our conditions, we expect a power deposition of the laser beam into the jetting sample of about 50%. Fig. 5(a) shows a comparison between Raman measurements recorded in jet and in a cuvette. The red curve shows a Raman spectrum of the $Cu(DMEGqu)_2PF_6$ sample in cuvette with a sample concentration of 10 mM, 19 mW laser power, and 15 min accumulation time. The blue curve shows a Raman spectrum that has been measured in a jet with 2 mM concentrated sample, 70 mW laser power, and 3 min accumulation time. For better comparison, the spectra have been normalized to laser power, sample concentration, accumulation time, and the irradiated volume.

The observed Raman signal in the jet (Fig. 5(a)) is enhanced approximately 27 times compared to the cuvette. Besides this, the sample peaks behavior in jet is clearly more pronounced than in the cuvette and allows a precise extraction of the information on the measured sample. We have achieved a significantly enhanced resolution of the Raman spectra as the source is defined by the jet diameter, which is magnified 6 times, yielding an effective slit image of only 60 $\mu$m, which is smaller than the effective image of the cuvette that is about 120 $\mu$m.

As a result of the signal improvements, time-resolved Raman measurements have become possible. In Fig. 5(b) we show a comparison between the difference spectrum of steady state Raman measurements of $Cu^I$ and $Cu^{II}$ (blue line) and an experimental difference in Raman spectrum at 50 ps delay time (red line). The experimental Raman spectrum has been recorded using a 3 $\omega$ beam with a pump energy of 4.38 eV (283 nm, FWHM = 1.7 ps, pulse energy = 1.29 nJ) and a 2 $\omega$ beam with a probe energy of 2.92 eV (425 nm, FWHM = 1.8 ps, pulse energy = 0.31 nJ). The effective laser power of the pump beam is 25 mW and the power of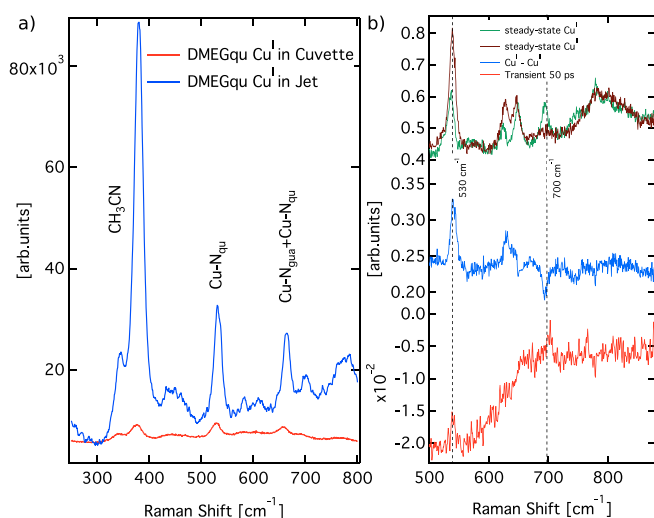 the probe beam is 23 mW. These values were recorded by a power meter in front of the entrance optics. To create a time delay of the pump and probe beam paths, a motorized delay line with 70 mm travel has been used. The position and time difference calibration of the observed delay has been measured with an UPD-30 fast photo diode (ALPHALAS GmbH) inside the entrance optics employing a 20 GHz Oscilloscope (Picoscope Modell 4312, Pico Technology). The overlap of spots of both lasers on the sample has been controlled using the periscope inside of the first monochromator of the UT-3 Raman spectrometer.[3] The theoretical difference spectrum has been created by the difference between the steady state Raman spectra of $Cu(TMGqu)_2PF_6$ (green) and $Cu(TMGqu)_2(OTf)_2$ (brown). Because of the Metal-to-Ligand-Charge-Transfer (MLCT) process, the oxidation state of copper changes during the excitation with the pump laser from $Cu^I$ to $Cu^{II}$. In Fig. 5(b) we can see that the peak structures of both spectra are similar. The relevant core vibration modes monitoring the structurally related catalytic activity of the complex at 530 cm$^{-1}$ and 700 cm$^{-1}$ are also clearly visible. These modes are difficult to observe as transient IR probes higher and transient THz probes lower energies.

In conclusion, we have developed a micro-jet based method to perform Raman measurements of bio-inorganic liquid samples that provide a significantly enhanced Raman signal compared to conventional methods. The samples can be delivered under vacuum conditions allowing control of their oxidation state. This method avoids sample damage effects by using a continuously replenished sample and requires a small amount of the sample for extensive measurements because we can match the diameter of the jet to the effective scattering volume. With a sample volume of 60 ml at a concentration of 2 mM, a typical flow rate of 70 $\mu$l/min, and with a jet diameter of 10 $\mu$m, a continuous measurement time of 15 h was possible. This consumed sample volume is small compared to the conventional liquid flow measurements. The behavior of the Raman signal on the jet size, sample concentration, and laser power have been shown to be linear. Furthermore, the micro-jet conditions can be controlled to allow transient Raman scattering to detect the structural dynamics of the sample.

FIG. 5. (a) Comparison between the steady-state Raman spectra of $Cu(DMEGqu)_2PF_6$ measured in the glass cuvette (red) and in the liquid jet (blue). For better comparison, the spectra were normalized to laser power, sample concentration, accumulation time, and the irradiated volume. Raman signal, observed in the jet is 27 times stronger than the signal in the cuvette. (b) Steady state Raman spectrum of $Cu(TMGqu)_2PF_6$ (green) and $Cu(TMGqu)_2(OTf)_2$ (brown) with a difference spectrum of $Cu(TMGqu)_2PF_6$ and $Cu(TMGqu)_2(OTf)_2$ (blue), experimental difference Raman spectrum at 50 ps delay time (red). The experimental Raman spectra are recorded with a pump energy of 4.38 eV and a probe energy of 2.92 eV.

[1]A. Hoffmann, S. Binder, A. Jesser, R. Haase, U. Flörke, M. Gnida, M. S. Stagni, W. Meyer-Klaucke, B. Lebsanft, L. E. Grünig *et al.*, "Catching an entatic state-a pair of copper complexes," Angew. Chem. Int. Ed. **53**, 299–304 (2014).

[2]P. Comba, M. Kerscher, and A. Roodt, "Slow electron self-exchange in spite of a small inner-sphere reorganisation energy: the electron-transfer properties of a copper complex with a tetradentate bispidine ligand," Eur. J. Inorg. Chem. **2004**, 4640–4645.

[3]H. B. Gray, Bo. G. Malmström, and R. J. P. Williams, "Copper coordination in blue proteins," J. Biol. Inorg. Chem. **5**, 551–559 (2000).

[4]M. Rolff, J. Schottenheim, H. Decker, and F. Tuczek, "Copper-O$_2$ reactivity of tyrosinase models towards external monophenolic substrates: molecular mechanism and comparison with the enzyme," Chem. Soc. Rev. **40**, 4077–4098 (2011).

[5]C. Citek, S. Herres-Pawlis, and T. D. P. Stack, "Low temperature syntheses and reactivity of Cu$_2$O$_2$ active-site models," Acc. Chem. Res. **48**, 2424–2433 (2015).

[6]S. Herres-Pawlis, R. Haase, P. Verma, A. Hoffmann, P. Kang, and T. D. P. Stack, "Formation of hybrid guanidine-stabilized bis($\mu$-oxo)dicopper cores in solution: Electronic and steric perturbations," Eur. J. Inorg. Chem. **2015**, 5426–5436.

[7]E. I. Solomon, R. K. Szilagyi, S. DeBeer George, and L. Basumallick, "Electronic structures of metal sites in proteins and models: contributions of function in blue copper proteins," Chem. Rev. **104**(2), 419–458 (2004).

[8]E. A. Lewis and W. B. Tolman, "Reactivity of dioxygen-copper systems," Chem. Rev. **104**(2), 1047–1076 (2004).

[9]E. I. Solomon, D. E. Heppner, E. M. Johnson, J. W. Ginsbach, J. Cirera, M. Oayyum, M. T. Kieber-Emmons, Ch. H. Kjaergaard, R. G. Hadt, and Li. Tian, "Copper active sites in biology," Chem. Rev. **114**, 3659–3853 (2014).

[10]Y. Matoba, T. Kumagai, A. Yamamoto, H. Yoshitsu, and M. Sugiyama, "Crystallographic evidence that the dinuclear copper center of tyrosinase is flexible during catalysis," J. Biol. Chem. **281**, 8981–8990 (2006).

[11]A. Bijelic, M. Pretzler, Ch. Molitor, F. Zekiri, and A. Rompel, "The structure of a plant tyrosinase from walnut leaves reveals the importance of "substrate-guiding residues" for enzymatic specificity," Angew. Chem. Int. Ed. **54**, 14677–14680 (2015).

[12]T. D. P. Stack, Dalton Trans., Chem. Rev. **2003**, 1881–1889.

[13]L. M. Mirica, M. Vance, D. J. Rudd, B. Hedman, K. O. Hodgson, E. I. Solomon, and T. D. P. Stack, "Tyrosinase reactivity in a model complex: an alternative hydroxylation mechanism," Science **308**, 1890–1892 (2005).

[14]E. I. Solomon and A. B. P. Lever, *Inorganic Electronic Structure and Spectroscopy, Volume I: Methodology* (Wiley, 2006), ISBN: 978-0-471-97124-5.

[15]B. Schulz, J. Bäckström, D. Budelmann, R. Maeser, M. Rübhausen, M. V. Klein, E. Schoeffel, A. Mihill, and S. Yoon, "Fully reflective deep ultraviolet to near infrared spectrometer and entrance optics for resonance Raman spectroscopy," Rev. Sci. Instrum. **76**(7), 073107 (2005).

[16]R. P. Saichu, I. Mahns, A. Goos, S. Binder, P. May, S. G. Singer, B. Schulz, A. Rusydi, J. Unterhinninghofen, D. Manske *et al.*, "Two-component dynamics of the order parameter of high temperature $Bi_2Sr_2CaCu_2O_{8+\delta}$ super- conductors revealed by time-resolved Raman scattering," Phys. Rev. Lett. **102**, 177004 (2009).

[17]K. R. Beyerlein, L. Adriano, M. Heymann, R. Kirian, J. Knoska, F. Wilde, H. N. Chapman, and S. Bajt, "Ceramic micro-injection molded nozzles for serial femtosecond crystallography sample delivery," Rev. Sci. Instrum. **86**, 125104 (2015).

[18]D. P. DePonte, U. Weierstall, K. Schmidt, J. Warner, D. Starodub, J. C. H. Spence, and R. B. Doak, "Gas dynamic virtual nozzle for generation of microscopic droplet streams," J. Phys. D. **41**, 195505 (2008).

[19]U. Weierstall, "Liquid sample delivery techniques for serial femtosecond crystallography," Philos. Trans. R. Soc., B **369**, 20130337 (2014).

[20]A. M. Gañán-Calvo, "Generation of steady liquid microthreads and micron-sized monodisperse sprays in gas streams," Phys. Rev. Lett. **80**, 285 (1998).

[21]E. J. Vega, J. M. Montanero, M. A. Herrada, and A. M. Gañán-Calvo, "Global and local instability of flow focusing: The influence of the geometry," Phys. Fluids. **22**, 064105 (2010).

[22]U. Weierstall, J. C. H. Spence, and R. B. Doak, "Injector for scattering measurements on fully solvated biospecies," Rev. Sci. Instrum. **83**, 035108 (2012).

[23]J. M. Montanero, A. M. Gañán-Calvo, A. J. Acero, and E. J. Vega, "Micrometer glass nozzles for flow focusing," J. Micromech. Microeng. **20**, 075035 (2010).

[24]A. M. Gañán-Calvo and J. M. Montanero, "Revision of capillary cone-jet physics: Electrospray and flow focusing," Phys. Rev. E **79**, 066305 (2009).

[25]A. J. Acero, C. Ferrera, J. M. Montanero, and A. M. Gañán-Calvo, "Focusing liquid microjets with nozzles," J. Micromech. Microeng. **22**, 065011 (2012).

[26]T. Si, F. Li, X.-Y. Yin, and X.-Z. Yin, "Modes in flow focusing and instability of coaxial liquid-gas jets," J. Fluid Mech. **629**, 1 (2009).

[27]M. Trebbin, K. Krüger, D. DePonte, S. V. Roth, H. N. Chapman, and S. Förster, "Microfluidic liquid jet system with compatibility for atmospheric and high-vacuum conditions," Lab Chip **14**, 1733 (2014).

[28]J. M. Montanero, N. Rebollo-Munoz, M. A. Herrada, and A. M. Gañán-Calvo, "Global stability of the focusing effect of fluid jet flows," Phys. Rev. E. **83**, 036309 (2011).

[29]A. Hoffmann, J. Stanek, B. Dicke, L. Peters, B. Grimm-Lebsanft, A. Wetzel, A. Jesser, M. Bauer, M. Gnida, W. Meyer-Klaucke *et al.*, "Implications of guanidine substitution on copper complexes as Entatic-State models," Eur. J. Inorg. Chem. **2016**, 4731–4743.

[30]E. Solomon and A. B. P. Lever, in *Electron Transfer Reactions*, edited by S. Isied (ACS, Washington, DC, 1997), Chap. 19.

[31]P. Comba, "Coordination compounds in the Entatic state," Coord. Chem. Rev. **200–202**, 217–245 (2000).

[32]B. L. Vallee and R. Williams, "Metalloenzymes: The entatic nature of their active sites," Proc. Natl. Acad. Sci. U.S.A. **59**, 498–505 (1968).